

Parametric Level-sets Enhanced To Improve Reconstruction (PaLEnTIR)

Ege Ozsar¹, Misha Kilmer², Eric de Sturler³, Arvind K. Saibaba⁴, Eric Miller¹ ‡

¹Department of Electrical and Computer Engineering, Tufts University, Medford, MA, USA

²Department of Mathematics, Tufts University, Medford, MA, USA

³Department of Mathematics, Virginia Tech, Blacksburg, VA, USA

⁴ Department of Mathematics, North Carolina State University, Raleigh, NC, USA

Abstract. We introduce PaLEnTIR, a significantly enhanced parametric level-set (PaLS) method addressing the restoration and reconstruction of piecewise constant objects. Our key contribution involves a unique PaLS formulation utilizing a single level-set function to restore scenes containing multi-contrast piecewise-constant objects without requiring knowledge of the number of objects or their contrasts. Unlike standard PaLS methods employing radial basis functions (RBFs), our model integrates anisotropic basis functions (ABFs), thereby expanding its capacity to represent a wider class of shapes. Furthermore, PaLEnTIR improves the conditioning of the Jacobian matrix, required as part of the parameter identification process, and consequently accelerates optimization methods. We validate PaLEnTIR’s efficacy through diverse experiments encompassing sparse and limited angle of view X-ray computed tomography (2D and 3D), nonlinear diffuse optical tomography (DOT), denoising, and deconvolution tasks using both real and simulated data sets.

Keywords: level-set, PaLS, parametric, reconstruction, tomography, piecewise constant

1. Introduction

Inverse problems are pivotal in a broad range of science and engineering applications. In the pursuit of extracting the unknown composition and structure of a medium from indirect observations governed by physical models, researchers often focus on characterizing “regions of interest” (ROIs). These ROIs may include features such as cancerous tumors in diffuse optical data [1], subsurface contaminants in hydrological data [2], or buried objects in electromagnetic data [3]. Conventionally, these problems typically involve a computationally intensive image formation step followed by ROI

‡ This research was supported by the U.S. National Science Foundation under awards 1720291, 1935555, 1934553, 1720398, and 1720305.

identification [4]. For problems where data are limited, the initial image formation stage will require potentially complex regularization methods to overcome ill-posedness. Alternatively, direct estimation of ROI geometry and contrasts from data offers a more efficient approach [5]. These *shape-based* methods are usually better-posed compared with pixel-based problems; however, topologically complicated shapes can lead to challenges [6]. For example, approaches based on using parametric shapes (circles, ellipsoids, etc.) to describe object geometry require that the number of components for the shape is known *a priori* or somehow estimated. For this and many other reasons [7], level-set methods have found great use for shape-based inverse problems because of their ability to naturally recover objects whose topology (number of connected components) is not known *a priori*.

Initially proposed by Osher and Sethian [8] for curve propagation modeling, level-set methods subsequently gained traction in solving inverse problems, as pioneered by Santosa [6]. Notable efforts have followed, employing level-set evolution techniques [9, 10], particularly in image processing [11]. For ill-posed problems, regularization of the level-set function becomes essential. Various strategies have emerged to address this, encompassing pixel-based approaches [12], geometric constraints [13], and finite-dimensional basis function spaces like the parametric level-set function (PaLS) concept. This latter approach, introduced for inverse problems by [7], is the basis for the work in this paper.

The PaLS model has proven to be capable of capturing the topological advantages of a level-set function while avoiding difficulties such as the need for explicit regularization and reinitialization that occur frequently when using traditional level-set methods for inverse problems. Moreover, it was shown in [7] that the low order representation of the inverse problem makes it possible to use Newton and quasi-Newton methods for determining the PaLS parameters. In recent works, the PaLS model in [7] and variants have been used across a range of application areas and imaging modalities including geophysics [14], seismology [15] and reservoir monitoring [16], image segmentation [17], tomography problems [18, 19, 20], electromagnetic imaging [21], and multi-modal imaging [22].

Despite the advantages of PaLS, room for improvement remains. Notably, existing PaLS models and most other level-set methods struggle to recover distributions of objects with multiple contrast values. Approaches like colour [23], vector [24], and binary level-sets [25] rely on a number of level-sets proportionate to the number of objects [17], leading to scalability challenges as the object count increases. Furthermore, the choice of basis functions for PaLS raises limitations. Traditionally, a weighted superposition of predetermined basis functions, predominantly radial basis functions (RBFs) [26, 27, 28], has been employed. However, RBFs possess only circular cross sections and thus can limit the range of objects that can be represented by the model and a given number of RBFs. Moreover, despite their efficacy, many prevailing PaLS models grapple with numerical conditioning issues. Models employing RBFs can encounter non-uniqueness in parameter representation due to infinitely many parameter pairs yielding the same

circular cross sections. As we illustrate empirically in this paper, this can yield ill-conditioned, even singular, Jacobian matrices — detrimental for quasi-Newton and even for trust-region methods, the performance of which degrades under such conditions [7].

Here, we develop Parametric Level-Sets Enhanced to Improve Reconstruction (PaLEnTIR) for piecewise constant image reconstruction to address the issues identified in the above paragraph. The specific contributions are as follows. First, we replace the binary Heaviside function used in the existing PaLS models with a smooth transition function. The resulting model can capture **multiple unknown contrasts with only a single level-set function**. Thus, the number of parameters to be estimated is independent of the number of contrasts. To the best of our knowledge, PaLEnTIR is the first level-set model with this property. The efficacy of this multi-contrast feature is contingent upon its capacity to specify space-varying bounds on the contrasts at relatively coarse scales. The new model achieves this by parametrically characterizing the spatially varying contrast limits on a sparse grid of points. Second, we replace the RBFs with anisotropic basis functions that produce rotated ellipsoidal cross-sections. This choice provides greater geometric flexibility and enhanced **shape expressiveness**. The model captures more detail while employing fewer basis functions, proving particularly advantageous for challenging scenarios like the representation of long, flat objects where RBFs encounter difficulties. Finally, we demonstrate empirically that bounding the expansion coefficients associated with the ABFs and fixing the centers of the basis functions significantly **improves the numerical performance** of the method, as evidenced by the reduction of the condition number of the Jacobian matrices generated over the course of the reconstruction process.

The organization of the paper is as follows. In section 2, we define our problem of interest and review the parametric level-set method. We also briefly discuss the nonlinear least-squares minimization algorithm, TREGS, used in our experiments, at the end of this section. In section 3, PaLEnTIR formulations for both 2D and 3D inverse problems are detailed. We also discuss the benefits of the new formulation relative to existing PaLS models. We demonstrate the benefits through a sparse view 2D X-ray computed tomography example. We provide experimental results for PaLEnTIR in section 4. Specifically, in subsection 4.1, we show the results for a 2D linear problem, namely deconvolution. In subsection 4.2, we demonstrate the performance of PaLEnTIR on limited angle view and sparse angle multi-contrast 2D inversion of the Radon transforms as well as a 3D limited angle view parallel beam tomography experiment. To test our approach on a nonlinear problem, in subsection 4.3, we show the experimental results of the new approach on diffuse optical tomography (DOT), a severely ill-posed inverse problem. Across this range of experiments, we use both real and synthetic data to show the robustness of our approach in a range of data-limited applications. Conclusions are provided in section 5.

2. Problem formulation

2.1. Forward and Inverse Problems

Consider a region of space to be imaged, $\Omega \subset \mathbb{R}^d$. For \mathbf{r} a point in Ω , let us define a spatially-dependent property $f(\mathbf{r})$ of the medium (e.g., electrical conductivity, optical absorption, sound speed, etc.). We denote with \mathcal{M} the map which takes $f(\mathbf{r})$ to a vector of noise free data. Typically, \mathcal{M} encompasses the physics of the sensing modality and the engineering details of the associated sensors. The data available for processing is equal to $\mathcal{M}(f)$ corrupted by noise. Unless specified otherwise, we assume that the noise is additive Gaussian. In summary, the forward model can be written

$$\mathbf{d} = \mathcal{M}(f) + \mathbf{w}, \quad (1)$$

where $\mathbf{w}, \mathbf{d} \in \mathbb{R}^{N_{pts}}$ represent the additive noise and the data available for processing.

The inverse problem requires determination of the unknown function f from \mathbf{d} . Following the penalized likelihood approach, (1) leads to the following minimization problem as the basis for recovering $f(\mathbf{r})$,

$$\min_f \frac{1}{2} \|\mathcal{M}(f) - \mathbf{d}\|_2^2 + \xi(f). \quad (2)$$

The first term in (2) arises from a Gaussian assumption on the noise and quantifies the mismatch error between model prediction and the data, while $\xi(f)$ is the regularization functional which is usually used when the problem is ill-posed and is chosen based on prior knowledge concerning, e.g., the degree of smoothness associated with f [29]. It is also possible to regularize the problem using a geometric parameterization of the unknown property. This is done by either embedding the regularization implicitly in the parameterization of the unknown property, in which case no explicit ξ may be needed, or by expressing it as geometric constraints on the shape of the unknown [9]. In this paper, we follow the former approach using a PaLS type of model.

2.2. Parametric Level-set methods

Under a PaLS model, $f : \mathbb{R}^d \rightarrow \mathbb{R}$ consists of object, O , and background, $\Omega \setminus O$, terms and is written as

$$f(\mathbf{r}) = f_O(\mathbf{r})\chi_O(\mathbf{r}) + f_B(\mathbf{r})(1 - \chi_O(\mathbf{r})), \quad (3)$$

where $f_O(\mathbf{r})$ and $f_B(\mathbf{r})$ are the generally spatially dependent property values of the object and background, respectively, and $\chi_O(\mathbf{r}) = 1$ for $\mathbf{r} \in O$ and 0 elsewhere is the characteristic function of the region O . Under this model, we seek O (or the boundary, ∂O), $f_O(\mathbf{r})$, and $f_B(\mathbf{r})$. As O can be multiply connected with each component having no specific (i.e., easily parameterized) shape, level-set methods have proven convenient

[7]. Mathematically, the level-set representation of O satisfies

$$\phi_O(\mathbf{r}) \begin{cases} > c & \mathbf{r} \in O, \\ = c & \mathbf{r} \in \partial O, \\ < c & \mathbf{r} \in \Omega \setminus O, \end{cases} \quad (4)$$

where c is a constant determining the level-set§ [7]. In terms of ϕ_O , $\chi_O(\mathbf{r}) = H(\phi_O(\mathbf{r}) - c)$ where $H(x)$ is the Heaviside function. Thus, (3) becomes

$$f(\mathbf{r}) = f_O H(\phi_O(\mathbf{r}) - c) + f_B (1 - H(\phi_O(\mathbf{r}) - c)) \quad (5)$$

where f_O and f_B are, for now, taken to be constants.

Many level-set methods follow a finite difference discretization of the level-set function, which requires a dense collection of nodes. The difficulty of implementing this approach as well as the numerical considerations of its discrete computation overshadow the advantages of the level-set function, especially in the case of ill-posed inverse problems [7, 30]. Alternatively, a parametric form for the level-set function expands $\phi_O(\mathbf{r})$ as a linear superposition of a set of basis functions (e.g., polynomial, radial basis function, trigonometric, etc). Specifically, the original PaLS model takes the form

$$\phi_{\text{rbf}}(\mathbf{r}; \mathbf{p}) = \sum_{j=1}^N \alpha_j \psi(\beta_j(\mathbf{r} - \boldsymbol{\chi}_j)), \quad \mathbf{p} := \begin{bmatrix} \boldsymbol{\alpha} \\ \boldsymbol{\beta} \\ \boldsymbol{\chi} \end{bmatrix}. \quad (6)$$

In this case, the PaLS function is formed as a weighted summation of N basis functions $\psi_j(\mathbf{r}) := \psi(\beta_j(\mathbf{r} - \boldsymbol{\chi}_j))$ for $j = 1, 2, \dots, N$. The basis functions $\psi_j(\mathbf{r})$ are often taken to be RBFs [31, 32, 33, 19]. We will refer to use of such basis functions as ‘‘RBF PaLS’’, and it is against such representations that we compare our new PaLEnTIR representation.¶ Each basis function $\psi_j(\mathbf{r})$ is associated with its own dilation coefficient β_j , and center location $\boldsymbol{\chi}_j$. Ignoring the contrasts f_B and f_O for a moment, \mathbf{p} contains the geometric unknowns to be determined, including $\boldsymbol{\alpha}$, $\boldsymbol{\beta}$, and $\boldsymbol{\chi}$, containing the expansion coefficients α_j , the dilation values β_j , and PaLS centers $\boldsymbol{\chi}_j \in \mathbb{R}^d$, respectively. In general, the length of this vector is $(d + 2)N$, which results in length $4N$ (for 2D problems) or $5N$ (for 3D).

Combining (6) with (5), we obtain $f = f(\mathbf{r}; \mathbf{p})$. The goal of a PaLS-based inverse problem is to recover the unknown \mathbf{p} based on the observed data \mathbf{d} and the model \mathcal{M} . In practice, this requires replacing the exact Heaviside function with a differentiable approximation (we discuss this more in section 3.1). If the contrast coefficients f_O and

§ This could be taken to be the zero level-set, though in [7], the case was made for c slightly larger.

¶ In [7], the norm in the argument is replaced by a pseudo-norm and $\psi(\cdot)$ is taken to be a compactly supported radial basis function. The compactness of the basis functions may be advantageous in terms of yielding a sparse Jacobian [7]. Here, we will use Gaussian RBFs instead of CSRBFs and forgo compactness in favor of retaining a norm, rather than a pseudo-norm. This choice facilitates the comparative analysis of the expressiveness and numerical properties of the proposed approach over RBF PaLS. The parameterization developed here and the analysis, can be utilized in a CSRBF framework.

f_B are known, the resultant inverse problem formulation using PaLS recovers f as $f(\hat{\mathbf{p}})$ where \mathbf{p} is a minimizer of a nonlinear least squares problem with the objective function

$$F(\mathbf{p}) = \frac{1}{2} \|\mathcal{M}(f(\mathbf{p})) - \mathbf{d}\|_2^2. \quad (7)$$

When the contrasts are not known, a cyclic descent method is often employed [34], in which one alternately estimates \mathbf{p} for the current estimates of f_O and f_B and then updates the contrasts using the just-computed PaLS parameters. For linear inverse problems, computing the contrasts is a linear least squares problem which can be solved efficiently, and the bulk of the computational effort is focused on estimating \mathbf{p} .

Since the number of PaLS basis functions is always much smaller than the size of the grid obtained from discretizing Ω , the PaLS parameterization acts as a form of regularization, so we can drop the regularization term $\xi(f)$ from the objective function.

In this paper, we use the TREGS algorithm to minimize (7) and solve for the PaLS parameters [35]. The TREGS algorithm is designed to address nonlinear least squares problems encountered in parameterized imaging scenarios. By analyzing spectral components of the Gauss–Newton direction, TREGS determines which components to discard or dampen, minimizing the total number of function and Jacobian evaluations. Leveraging the Basic Trust Region Algorithm [36], TREGS guarantees global convergence to a critical point, making it a robust optimization tool. The algorithm employs a discrepancy principle–based stopping criterion. The discrepancy principle states that one should stop iterating when the norm of the residual reaches the norm of the (weighted) noise vector [37]. In our experimental setup, an additional stopping criterion is implemented to prevent unnecessary computational expenditure. Specifically, the algorithm concludes its iterations when the relative decrease in the residual falls below a predefined threshold, ensuring judicious use of computational resources.

3. Parametric Level-sets Enhanced To Improve Reconstruction

In this section, we introduce PaLEnTIR, and we discuss its advantages over the RBF PaLS representation. The proposed PaLEnTIR model is defined as follows

$$f(\mathbf{r}; \mathbf{p}) = C_H(\mathbf{r})T(\phi(\mathbf{r}; \mathbf{p})) + C_L(\mathbf{r})(1 - T(\phi(\mathbf{r}; \mathbf{p}))), \quad (8)$$

$$\phi(\mathbf{r}; \mathbf{p}) = \sum_{j=1}^N \sigma_h(\alpha_i) \psi(\mathbf{R}_j(\mathbf{r} - \boldsymbol{\chi}_j)), \quad \mathbf{p} := \begin{bmatrix} \boldsymbol{\alpha} \\ \boldsymbol{\beta} \\ \boldsymbol{\gamma} \end{bmatrix}. \quad (9)$$

As explained below, the N matrices, $\mathbf{R}_j := \mathbf{R}(\boldsymbol{\beta}_j, \boldsymbol{\gamma}_j)$, for $j = 1, 2, \dots, N$, depend on the $\boldsymbol{\beta}$ and $\boldsymbol{\gamma}$ sub-vectors of \mathbf{p} , respectively. The length of vector \mathbf{p} is $3N$ (for 2D) or $7N$ (for 3D). T is the new transition function, replacing the Heaviside function, $C_H(\mathbf{r})$ and $C_L(\mathbf{r})$ are the new “contrast coefficients”, replacing f_O and f_B in (5), and $\sigma(\cdot)$ is a function to bound the values of α_i . Compared to (6), the PaLEnTIR model in (8) enhances PaLS in the following ways, each of which is discussed in depth in the following subsections:

- A) **Multi-contrast, single level-set** reconstructions are obtained by: (a) Replacing the Heaviside function with the smooth transition function $T_w : \mathbb{R} \rightarrow (0, 1)$; and (b) Relabeling and reinterpreting $f_O(\mathbf{r})$ and $f_B(\mathbf{r})$ as upper and lower contrast bounds, C_H and C_L . In the simplest case, where there is a single object in the field, these are constant. For the problems of interest in this paper, both C_L and C_H are functions of space, whose structures and parameterization are discussed in subsection 3.1.
- B) **Shape-expressiveness** is expanded by replacing the scalar dilation coefficient, β_j in PaLS, by a matrix \mathbf{R}_j , implementing what we call stretching and sliding. For 2D problems, each \mathbf{R}_j depends on one element of $\boldsymbol{\beta}$ and one of $\boldsymbol{\gamma}$ for a total of 2 parameters per basis function. In the 3D case, this changes to three β 's and three γ 's per \mathbf{R}_j , for a total of 6 parameters per basis function.
- C) **Numerical performance** is improved by (a) Fixing the basis function centers on a grid of pre-specified points, $\boldsymbol{\chi}_j$, so that these quantities are no longer estimated as part of the inversion process, and combined with the new parameterization, reducing the dimension of the search space; (b) Constraining the size of the expansion coefficients using a function $\sigma_h(\alpha_i) \in (-1, 1)$; and (c) Replacing RBFs, that have non-unique mapping of parameters to c -level-sets, with the new anisotropic basis functions (ABFs).

We next discuss each of these three enhancements in turn.

3.1. Multi-contrast, Single Level-set Reconstructions

In the previous section, we assumed that the property function $f(\mathbf{r})$ had a binary structure, i.e., each point in Ω either belongs to the region O or the background. However, it may well be the case that we have to represent regions containing objects with more than two contrast values [38, 39, 40]. To solve this problem, we replace the Heaviside function in the original PaLS model with a transition function $T(x)$ which smoothly, and monotonically varies between zero and one. Specifically, in this paper we take

$$T(x) = \frac{1}{2} \left[1 + \frac{2}{\pi} \tan^{-1} \left(\frac{\pi(x-c)}{w} \right) \right], \quad (10)$$

where w determines the steepness of the transition region. The approximate Heaviside function used in the original PaLS work also monotonically increased from zero to one [7] and thus is similar to $T(x)$. The difference lies in the width of the transition. As seen in Figure 1a, for the approximate Heaviside function, the transition region is by construction very narrow, as the goal was to represent binary valued objects, whose “phases” are separated by a narrow, smooth interface. In the new formulation, we stretch the width of this transition region, so that $f(\mathbf{r})$ can assume basically *any* value between C_L and C_H , as seen in Figure 1b.

To illustrate the impact of these changes to the PaLS model, in Figure 2a, we display an image of size 256×256 pixels, comprised of five piecewise constant objects on a zero-contrast background. Here, we took the forward model to be the identity, so

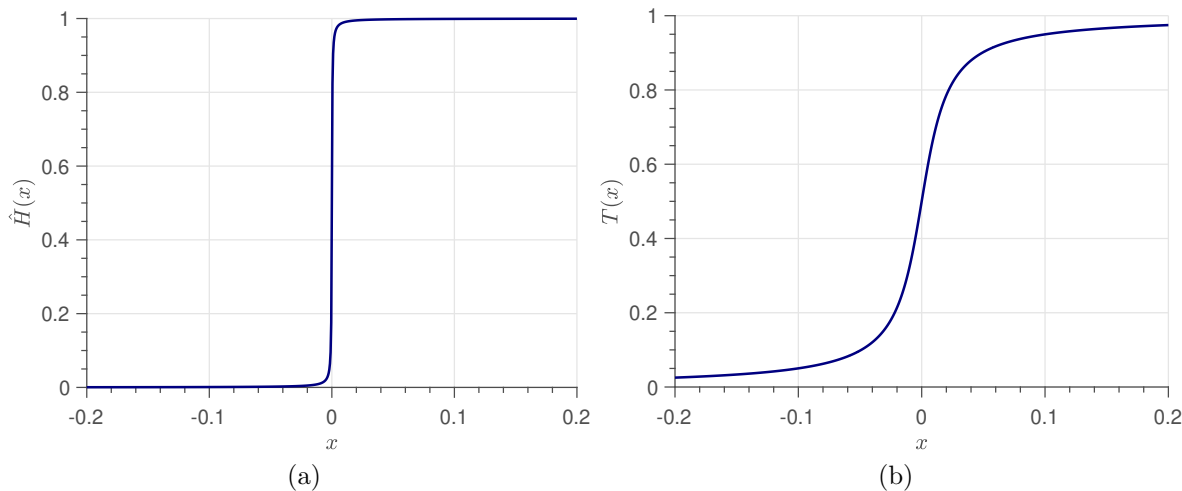


Figure 1: (a) The plot of the approximate Heaviside function $\hat{H}(x)$ for the zero level-set ($c = 0$). (b) The plot of the new transition function $T(x)$ for zero level-set.

that $\mathbf{d} = \mathbf{f}(\mathbf{p}) + \mathbf{w}$, where $\mathbf{f}(\mathbf{p})$, a discrete representation of $f(\mathbf{r}; \mathbf{p}, C_H, C_L)$, is a vector of length $N_{pts} = 256^2 = 65536$ obtained using the discretization process described in section 4. The vector \mathbf{w} contains independent, identically distributed Gaussian random variables, with variance such that the signal to noise ratio (SNR) of the corrupted image is 22 dB. In this paper, SNR is calculated as

$$\text{SNR}_{\text{dB}} = 20 \log_{10} \left(\frac{\sqrt{\sum_{n=1}^{N_{pts}} |d_n|^2}}{\sqrt{\sum_{n=1}^{N_{pts}} |w_n|^2}} \right) \quad (11)$$

where d_n and w_n are the n^{th} element of the noise-free data and the noise, respectively. The image corrupted with additive Gaussian noise is shown in Figure 2b, along with our PaLEnTIR reconstruction in Figure 2c. We used 225 basis functions centered on an equally spaced 15×15 grid. Each basis function requires the parameters α , β and γ , resulting in total of $3N$ (675) parameters for N (225) basis functions. Contrast coefficients are chosen as $C_H = 1$ and $C_L = 0$, since the maximum contrast in the image is equal to 1 and the minimum is equal to 0.

In Figure 2c, we see that the bright yellow region, whose contrast is equal to C_H , is recovered most accurately among the objects. The α_i of the basis functions in this region take on relatively large values which are truncated by $T(x)$. The regions without objects are also recovered very accurately. In those areas the coefficients are relatively small, so that the transition function $T(x)$ creates a constant, zero-background. For the remainder of the structures whose contrasts are between 0 and 4, we see blurred edges and oscillations similar to what we would expect from least squares denoising. Overall, the use of T_w resulted in accurate recovery of regions with values not between C_H and C_L , and rough recoveries of both shapes and contrasts of regions with values in between C_H and C_L . This is achieved through the utilization of a single level-set, requiring only

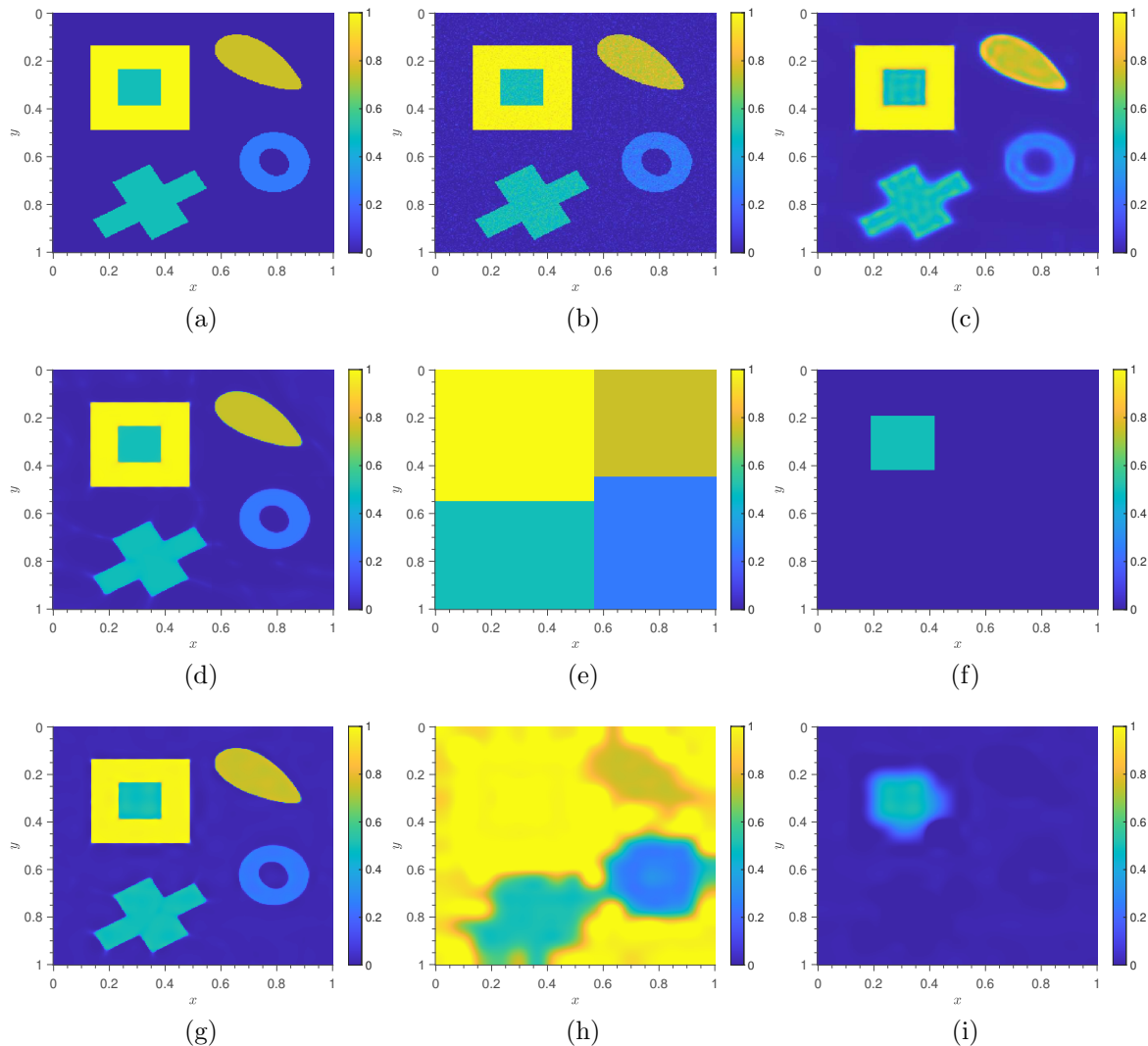


Figure 2: (a) Image of size 256×256 pixels comprised of five piecewise constant objects with different shapes and contrasts on a zero-contrast background. (b) The image corrupted with additive Gaussian noise (SNR: 22dB). (c) PaLEnTIR recovery of the image with fixed contrast limits. (d) PaLEnTIR recovery using manually adjusted vectors (e) \mathbf{C}_H and (f) \mathbf{C}_L . (g) PaLEnTIR recovery with the parameterized contrast limits, $\mathbf{p}_c \in \mathbb{R}^{2N}$, included in the estimation problem. Estimated parameterized contrast limits (h) $C_H(\mathbf{r})$ and (i) $C_L(\mathbf{r})$.

675 unknowns, despite dealing with an 65536-pixel image.

The strong results in Figure 2c for the background and the yellow object in the upper left corner arise from the ability of the transition function to truncate the values of ϕ which are not between C_H and C_L . More generally, PaLEnTIR can achieve similar results across the entire scene by varying C_H and C_L in space. For example, consider the case where we set $C_H(\mathbf{r})$ and $C_L(\mathbf{r})$ as shown in Figures 2e and 2f. Re-estimating \mathbf{p} with these distributions of $C_H(\mathbf{r})$ and $C_L(\mathbf{r})$ yields the results in Figure 2d, where we

now see near-perfect recovery of all objects and the background.

The results in Figure 2d and the associated discussion illustrate the ability of the PaLEnTIR model to recover piecewise constant scenes comprised of objects with more than two contrasts using a single level-set function. This feature rests heavily on the ability to specify space-varying bounds on the contrasts at relatively coarse scales. The key issue is to do this in a way that retains the advantages of a PaLS-type model: low-order and no need for explicit regularization. This is accomplished by parameterizing $C_H(\mathbf{r})$ and $C_L(\mathbf{r})$, the spatially varying contrast limits, using bi-cubic (tri-cubic for 3D) interpolation [41, 42] (via the Matlab function “*imresize*”). In addition to α, β, γ , for each basis function, we add 2 new parameters, which we refer as p_H and p_L , for upper and lower contrast bounds respectively. Consequently, for a PaLEnTIR model with $n_B \times n_B$ basis functions, where $n_B = \sqrt{N}$, there are two N -vectors of parameters, referred as \mathbf{p}_H and \mathbf{p}_L . To see the impact of parameterizing the contrast limits, we repeat the same experiment with the same \mathbf{w} to recover the multi-contrast objects in Figure 2a. For the initial values of \mathbf{p} , we use the previously estimated PaLEnTIR parameters, which represent the image in Figure 2c, and we initialize \mathbf{p}_H and \mathbf{p}_L to ones and zeros respectively and rerun the TREGS algorithm. Figure 2g shows the resultant PaLEnTIR representation. The number of estimated parameters is increased from 675 to only 1125, still significantly fewer than the number of pixels in the represented image, which is 65536. As seen in Figure 2g, the new model with parameterized contrast limits has recovered all objects and the background accurately with near-perfect sharp boundaries, and maintains smooth piecewise constant contrasts everywhere. The contrast limits produced with the estimated $\mathbf{p}_c = [\mathbf{p}_H; \mathbf{p}_L]$, are shown in Figures 2h and 2i. The estimated contrast limits capture the contrast values of the objects at a relatively coarse scale. Noticeably, they look very similar to the handcrafted $C_H(\mathbf{r})$ and $C_L(\mathbf{r})$ in Figures 2e and 2f, especially at or near where the objects are located.

3.2. Advancements in the shape-expressiveness

While radial basis functions (RBFs) provide flexibility in terms of shape representation for PaLS, they are limited by the fact that they possess only circular, in 2D, or spherical, in 3D, level-sets, making them inefficient for representing, e.g., highly anisotropic shapes [22]. Motivated by these observations, we replace the RBFs in the old PaLS [7] with a model of the form

$$\psi(\mathbf{r}) = e^{-\|(\mathbf{R}(\mathbf{r}-\mathbf{x}))\|_2^2}, \quad (12)$$

where \mathbf{R} is a 2×2 matrix for 2D problems and 3×3 for 3D problems. As in [22], this model produces elliptical cross sections; however, the parameterization of \mathbf{R} is new and requires fewer parameters. We discuss the 2D and 3D cases separately.

In the 2D case, we define

$$\mathbf{R} = \mu \begin{bmatrix} e^\beta & \gamma \\ 0 & e^{-\beta} \end{bmatrix}, \quad (13)$$

where as shown below, β and γ define the eccentricity and orientation of the elliptical level-sets, while μ impacts the scale of the ellipses. In this paper, β and γ are parameters to be determined, while μ is fixed. To elucidate the role of these parameters, we consider the $N = 1$ case for both PaLS and PaLEnTIR. We define the c -level-set representation of a curve Γ as $\Gamma = H(\phi(\mathbf{r}, \mathbf{p}) - c)$. That is, Γ is the set of points \mathbf{r} such that $\phi(\mathbf{r}; \mathbf{p}) = c$ with $c > 0$:

$$\Gamma = \{(x, y) \in \mathbb{R}^2 \mid \phi(x, y; \mathbf{p}) = c\}. \quad (14)$$

We begin by examining the PaLS c -level-set of a single RBF centered at the origin:

$$\phi_{\text{rbf}}(x, y, \alpha, \beta) = \alpha e^{-\beta(x^2+y^2)}. \quad (15)$$

With ϕ_{rbf} in (14) and $c > 0$, we require $\alpha > 0$ as well to obtain a nonempty shape. Simple algebra gives

$$\Gamma_{\text{rbf}} = \left\{ (x, y) \in \mathbb{R}^2 \mid x^2 + y^2 = \frac{1}{\beta} \ln \frac{\alpha}{c} \right\}. \quad (16)$$

As anticipated, (16) defines a circle with radius $\sqrt{\frac{1}{\beta} \ln \frac{\alpha}{c}}$. We emphasize here that, with c fixed, there are an infinite number of (α, β) pairs that will give the same circle.

Next, we consider the $N = 1$ PaLEnTIR c -level-set where $\phi(x, y, \alpha, \mathbf{R}) = \sigma_h(\alpha) \exp(-\|\mathbf{R}\mathbf{r}\|_2^2)$ with $\mathbf{r}^T = [x \ y]$. In this paper, we take $\sigma_h(\alpha) = \tanh \alpha$. Notice that $\sigma_h(\cdot)$ bounds the weight coefficient of the basis function between -1 and 1 and is discussed in greater depth in section 3.3. Using this ϕ in (14) and $c > 0$, a non-empty Γ requires $\sigma_h(\alpha) > 0$ and thus $\alpha > 0$. Dividing both sides by $\sigma_h(\alpha)$ and taking the logarithm yields

$$\Gamma_{\text{new}} = \left\{ (x, y) \in \mathbb{R}^2 \mid (e^\beta x + \gamma y)^2 + e^{-2\beta} y^2 = \tau^2 \right\} \quad (17)$$

with $\tau^2 = \frac{1}{\mu^2} \ln \frac{\sigma_h(\alpha)}{c}$. When β and γ are 0, similar to Γ_{rbf} , Γ_{new} is a circle with a radius of τ . As $0 < \sigma_h(\alpha) \leq 1$, we see that μ and c define the largest circle representable using PaLEnTIR. While it may be useful to estimate one or both of these quantities along with the other model parameters, here we choose them to be constants. Specifically, c is set to 0.01, a value slightly larger than 0, for the reasons discussed in [7], and μ is set to 10 to have the maximum area of a single ABF to be slightly less than 15% of the total area, to restrict the extent to which the ABFs overlap each other.

When β and γ are nonzero, the Γ_{new} curve becomes elliptical. To understand the role of each parameter in defining the geometry of the ellipse, we start by viewing \mathbf{R} as the Cholesky factor of the symmetric positive definite (SPD) matrix $\mathbf{A} = \mathbf{R}^T \mathbf{R}$, which we call the *Stretch and Slide Matrix*. This matrix includes two types of parameters which are estimated by the PaLEnTIR reconstruction: the *stretching* parameter β and the *sliding* parameter γ . In Figure 3a, the impact of the *stretching* parameter β is shown. With $\gamma = 0$, nonzero values of β produce ellipses with principle axes in the x and y directions. We visualize the impact of increasing β as someone holding the circle

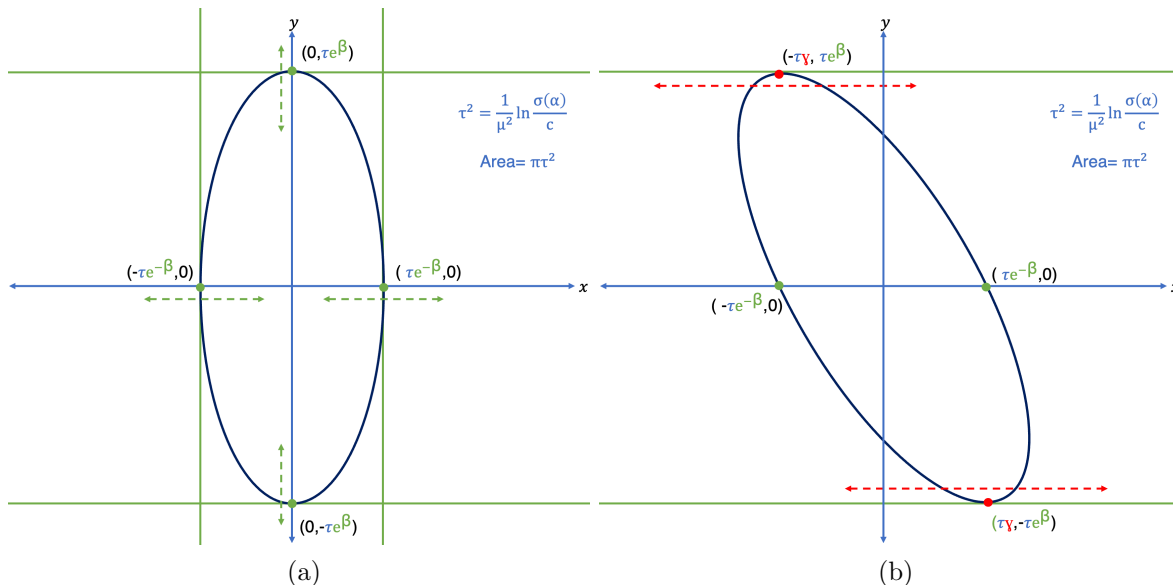


Figure 3: The impact of the parameters on the c -level ellipsoidal representation of the new basis function. (a) shows the impact of the *stretching* parameter β and (b) shows the impact of the *sliding* parameter γ .

(assuming $\beta = 0$ initially) at two opposite points touching the x and y axes (points shown with green dots in Figure 3a), and stretching in the direction of green dashed arrows. We call this shape transformation “stretching,” and hence β the *stretching* parameter. Similarly, as shown in Figure 3b, γ is the *sliding* parameter, because increasing γ horizontally “slides” the maximum and the minimum points of the ellipse along the vertical axes, as shown in with red dashed arrows. Since the determinant of \mathbf{A} is μ^2 , these two shape transformations do not change the area of the ellipse. The area depends on the constants μ , c , and the parameter α . In summary, with c and μ fixed, α controls the total area by homogeneously expanding the shape, β controls the upper and lower tangent lines by stretching the ellipse, and γ slides the tangent points of the ellipse along the tangent lines.

If we compare (16) and (17), we can clearly see that the β in ϕ_{rbf} , which adjusts the scale of the circles, is replaced with μ^2 . As we explained above, the parameters α and β in ϕ_{rbf} have a related (but opposite) effect on the c -level-set, and infinitely many pairs (α, β) exist that give the same Γ_{rbf} . Hence, we replaced the β in ϕ_{rbf} with a fixed constant μ^2 to reduce the dimension of the search space of the model and use only the parameter α to determine the scale of the ellipses.

To demonstrate the extended capacity for shape representation in PaLEnTIR, we compare PaLEnTIR and RBF PaLS on a 2D X-ray computed tomography (CT) test problem. Utilizing an open-access data set of tomographic X-ray data, featuring a carved cheese specimen [43], the reference image produced through high-resolution filtered back-projection (FBP) reconstruction, yielding a 2000×2000 pixel representation,

is illustrated in Figure 4a. Focusing on a sparse view problem with 15 projections spanning the full 360 degree circle, both PaLEnTIR and RBF PaLS configurations used 8×8 basis functions. Additionally, both models featured fixed values for the contrast coefficients, C_H and C_L for PaLEnTIR and f_O and f_B for RBF PaLS, set to 0.007 and 0, respectively. The recovered images of 128×128 pixels, are shown in Figures 4b and 4c. As discussed earlier, using the new ABFs introduces greater adaptability in shape representation, allowing for the capture of finer details with the same number of basis functions, and in fact reducing the total number of unknowns as well. In 2D, for N basis functions, RBF PaLS requires $4N$ parameters, α_j , β_j , and χ_j , for $j = 1, 2, \dots, N$. Whereas, for N basis functions PaLEnTIR requires only $3N$ parameters, α_j , β_j , and γ_j . The results underscore the advantages of PaLEnTIR, as it exhibits a more detailed recovery, discerning subtle features that are not captured in the RBF PaLS representation. For instance, the small hole on the left side of the carved letter “C” is effectively captured in the PaLEnTIR recovery, albeit not perfectly, while the hole cannot be observed in the RBF PaLS recovery. Similarly, when analyzing the carved letters “C” and “T,” the curved edges and fine details are more faithfully restored in the PaLEnTIR representation, while they are smeared out in the RBF PaLS recovery. Overall, RBF PaLS was able to recover the main body of the cheese and the background, but the recovery of the carved letters is rough. On the other hand, *with the same number of basis functions and fewer (64 less) parameters*, PaLEnTIR recovers significantly more details on the carved letters and even the small details on the cheese, which are absent from the RBF PaLS recovery.

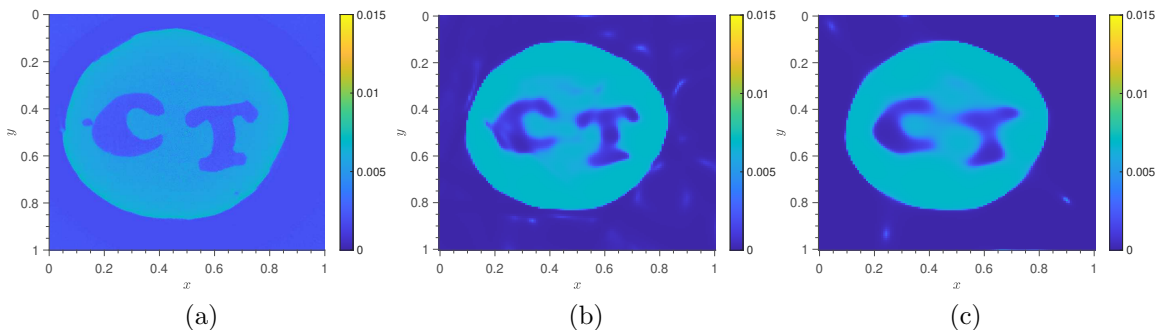


Figure 4: (a) Reference image of a carved cheese specimen computed using a high-resolution filtered back-projection (FBP) from the 360-projection sinogram. (b) PaLEnTIR recovery from the tomographic X-ray data using only 15 projections. (c) RBF PaLS recovery using the same data as PaLEnTIR.

For the 3D case, we construct $\mathbf{R}_3 \in \mathbb{R}^{3 \times 3}$ using three stretch and slide matrices as

follows

$$\mathbf{R}_3 = \mu \begin{bmatrix} e^{\beta_1} & \gamma_1 & 0 \\ 0 & e^{-\beta_1} & 0 \\ 0 & 0 & 1 \end{bmatrix} \times \begin{bmatrix} 1 & 0 & 0 \\ 0 & e^{\beta_2} & \gamma_2 \\ 0 & 0 & e^{-\beta_2} \end{bmatrix} \times \begin{bmatrix} e^{\beta_3} & 0 & \gamma_3 \\ 0 & 1 & 0 \\ 0 & 0 & e^{-\beta_3} \end{bmatrix}.$$

Note there are six parameters in our model, with each of the three matrices in the product affecting a shear transformation in a 2D plane within \mathbb{R}^3 . Similar to 2D case, \mathbf{R}_3 creates anisotropy in x, y, z and, assuming all three β_i are finite, may be viewed as the Cholesky factor of the symmetric positive definite (SPD) matrix $\mathbf{A} = \mathbf{R}_3^T \mathbf{R}_3$. We note that in the 3D PaLS model in [22], the authors modify the CSRBF formulation to use a matrix-based dilation to define ellipsoids. Unlike what we propose here, their method uses a symmetric 3×3 matrix, parameterized by the six unique elements of such a structure. One of the advantages of our formulation is that $\mathbf{R}_3^T \mathbf{R}_3$ is always SPD, whereas in the 3D PaLS model in [22] regularization is required to enforce this constraint.

3.3. Numerical improvements and stability

As we detail below, relative to RBF PaLS, PaLEnTIR exhibits enhanced numerical performance through several key modifications: (a) a reduction in the number of parameters achieved by fixing the centers of the Anisotropic Basis Functions (ABFs); (b) the introduction of the $\sigma_h(\cdot)$ function to ensure that the values of α_i are bounded; and (c) alterations to the basis functions, ensuring uniqueness in the parametric representation of shapes by a better choice of basis functions.

In contrast to RBF PaLS, which requires adjusting RBF centers due to the limited shape expressiveness of RBFs, PaLEnTIR exhibits enhanced shape expressiveness with anisotropic basis functions (ABFs) using fixed and homogeneously distributed centers. This not only eliminates the need for center estimation during inversion but also reduces the dimension of the search space, contributing to numerical improvements.

Here, we use the condition number of the Jacobian matrix to quantify numerical performance. Recall that the condition number measures the sensitivity to perturbations of the solution to a linear system of equations. As discussed in [44, 45], this is a crucial metric in determining the performance of a Newton-type approach to the estimation of the model parameters. We define the condition number of the Jacobian as the ratio of the largest to smallest singular value. Values of the condition number near 1 indicate a well-conditioned matrix, and large values indicate an ill-conditioned matrix. The expressions detailing the derivatives of the PaLEnTIR parameterization with respect to model parameters, which are necessary for the derivation of the Jacobian, are provided in the Appendix A. Note that we are solving a least squares problem, so the condition number of the least squares problem is not just the ratio of singular values of the matrix but the residual.

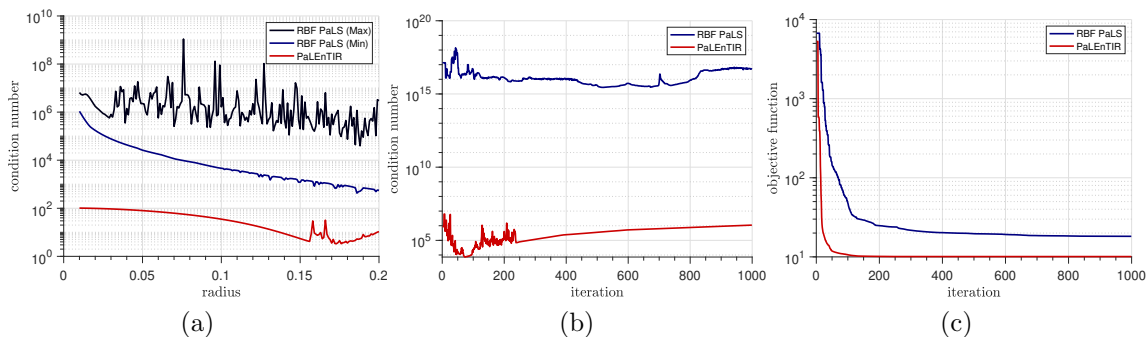


Figure 5: (a) Condition number of the residual versus the radius of circular cross sections (corresponding to appropriate level sets) for the two models. The black line (Max) and blue line (Min) represent RBF PaLS; the red line represents PaLEnTIR. (b) Condition number of the residual versus TREGS iterations, and (c) objective function plots over TREGS iterations of the 2D sparse view tomographic X-ray experiment. Blue line is for RBF PaLS and red line is for the new PaLEnTIR. The resultant reconstructions are shown in Figures 4b and 4c.

Similar to the discussion in subsection 3.2, our initial focus is on the single-basis function scenario. Given that RBF PaLS is confined to generating circular cross-sections (see section 3.2), we evaluate the numerical performance of both models in terms of their condition numbers, when their respective basis functions shape identical circles in their c -level-set representations, and the forward model is taken to be the identity in a noise-free case. Figure 5a plots the condition number against the radius of the circular cross-sections for both RBF PaLS and PaLEnTIR models. Given that the leading coefficient of PaLEnTIR limits the size of produced shapes, we focus on circular cross-sections with radii ranging from 0.01 to 0.2 units within a square region of 2 units per side. The condition number is computed using the function "cond(.)" in Matlab. Unlike PaLEnTIR, RBF PaLS can produce the same cross-section with many (α, β) pairs. Consequently, we produce identical cross-sections for radii ranging from 0.01 to 0.2, with increments of 0.001. We vary (α, β) pairs, increasing α by 0.01 within the range of 0.01 to 1. For each radius, we plot both the minimum and maximum condition numbers. The black and blue lines represent the maximum and minimum condition numbers for RBF PaLS, respectively, and the red line represents the condition number for PaLEnTIR. Notably, even if specifically selecting the (α, β) pairs that yield the minimum condition number for RBF PaLS, this is still much larger than the condition number obtained with PaLEnTIR. In the *worst* case scenario for RBF PaLS, where we pick the (α, β) pairs with the largest condition number for each cross section radius, the condition number is significantly larger than for PaLEnTIR.

Next, we turn our attention to evaluating the numerical performance for a 2D X-ray computed tomography experiment, as detailed in subsection 3.2. Figures 5b and 5c plot the condition number and the objective function (or misfit) against the

number of TREGS iterations, respectively. In both plots, the black line represents RBF PaLS, while the blue line represents PaLEnTIR. Figure 5b clearly shows the superior conditioning achieved by PaLEnTIR, confirming the results observed in the single-basis function case. This analysis is conducted with an 8×8 grid of basis functions for a real sparse-view X-ray CT problem. Additionally, Figure 5c highlights two noteworthy enhancements in PaLEnTIR. Firstly, PaLEnTIR attains significantly better objective function values, supporting the observations drawn from Figures 4b and 4c in the previous subsection. Secondly, the PaLEnTIR parameterization leads to better solutions (smaller objective function values) in substantially fewer iterations compared with the RBF PaLS parameterization, leading to a substantial improvement in numerical performance as well.

4. Experimental evaluation

We explore the utility of PaLEnTIR using a variety of linear and nonlinear forward models, particularly for problems where the data are limited. All experiments require that we use a discrete form of the forward model developed in section 2. To keep the discussion simple, we use quadrature rules for all integral operators and finite differences if the forward operator involves a PDE. We could use other methods of discretization, but these assumptions permit a straightforward extension of the continuous to discrete notation for purposes of this paper; that is, the vector of unknowns represents the values of the desired function $f(\mathbf{r}; \mathbf{p})$ at a finite set of grid points. Specifically, let \mathbf{r}_i , for $i = 1, \dots, N_{pts}$, denote a discrete set of 2D or 3D spatial grid points in Ω . We define the N_{pts} -vector $\mathbf{f}(\mathbf{p})$ as $[\mathbf{f}(\mathbf{p})]_i = f(\mathbf{r}_i; \mathbf{p})$. In this discrete case, $\mathcal{M}(\mathbf{f}(\mathbf{p}))$ represents the measured data for all sources given the discrete values $f(\mathbf{r}_i; \mathbf{p})$. The discrete forward model thus becomes

$$\mathbf{d} = \mathcal{M}(\mathbf{f}(\mathbf{p})) + \mathbf{w}. \quad (18)$$

We compare the performance of the PaLEnTIR model with that obtained using the L2-Total Variation (TV) regularization. For the TV method we use TVReg in [46]. As a distinct advantage over pixel-based methods, PaLEnTIR eliminates the need for a regularization parameter, in contrast to the TV method, where selecting a regularization parameter is essential. *In this paper, we always choose the TV regularization parameter that results in the minimal Mean Squared Error (MSE) when comparing with PaLEnTIR. This ensures that the TV result used in the comparison represents the best-case scenario, which generally would not be achievable in practice.* The number of unknowns employed by PaLEnTIR in our experiments is quite modest in comparison with the necessary number of unknowns for the TV method. For N ABFs, PaLEnTIR employs $3N$ (for 2D) or $7N$ (for 3D) PaLS parameters, and additionally $2N$ contrast parameters. Consequently, the parameter vector \mathbf{p} of PaLEnTIR is of size $5N$ (for 2D) or $9N$ (for 3D). On the other hand, L2-TV regularization is a pixel-based method and the number of unknowns is equivalent to the number of pixels in the discretized image. Note that number of parameters for PaLEnTIR is independent of the

resolution and depends only on the number of basis functions, one of the key advantages of PaLS-type methods.

We show results for both PaLEnTIR and TV methods and compare them based on the following metrics: PSNR (dB), SNR (dB), SSIM, and MSE. The Structural Similarity Index (SSIM) was created to replicate the human visual perception system [47]. A value closer to 1 indicates that the two images are very similar, whereas a value closer to -1 indicates the opposite. Mean Squared Error (MSE) is a commonly used metric to quantify the difference in the values of corresponding pixels between the sample and the reference images. PSNR is a commonly used metric to quantify the signal quality by comparing the peak level of a desired signal to the level of noise.

4.1. Deconvolution

Deconvolution is a linear inverse problem that recovers a desired signal from its convolution with a filter or a distortion function associated with an instrument or the physics of the problem. The discrete forward model is defined as in (18) with $\mathbf{f}(\mathbf{p})$ as in (8), giving the forward mapping $\mathcal{M}(\mathbf{f}(\mathbf{p})) = \mathbf{A}\mathbf{f}(\mathbf{p})$. The matrix \mathbf{A} comes from discretizing an integral equation that represents convolution.

In our deconvolution experiment, we seek to reconstruct a 256×256 image from input data that has been both filtered and corrupted by noise. The data is generated by convolving the authentic image with a rotationally symmetric Gaussian low-pass filter of size 5×5 with standard deviation 1, using the MATLAB function `fspecial` with default parameters. Subsequently, the data is contaminated with 10% additive Gaussian white noise, resulting in a data SNR of 22dB, as illustrated in Figure 6a. We use 225 basis functions in a 15×15 grid resulting in 1125 unknown parameters. This results in a reduction of more than 98% in the number of unknowns compared with the 256×256 array of pixels comprising the underlying discretization of the image domain. Figure 6b shows the PaLEnTIR recovery, and Figure 6c shows the TV recovery. Table 1 shows the performance metrics of both recoveries; the best results are shown in bold font. PaLEnTIR performs better across all 4 metrics, while requiring relatively few unknowns. The larger PSNR and SNR and smaller MSE values indicate that PaLEnTIR outperforms TV in terms of minimizing the absolute error. Furthermore, according to the SSIM scores, the perceptual difference between the original image and the TV recovery is larger than that for PaLEnTIR, which suggests that compared with TV, the PaLEnTIR recovery exhibits a closer resemblance to the ground truth image. Upon reviewing Figures 6b and 6c, it is evident that PaLEnTIR demonstrates a strong performance in delineating object boundaries, while the TV recovery exhibits some blurriness along several boundaries. Additionally, a close inspection of the TV recovery of the ring-shaped object reveals challenges in accurately representing the object’s boundary and shape, resulting in a slightly coarse representation.

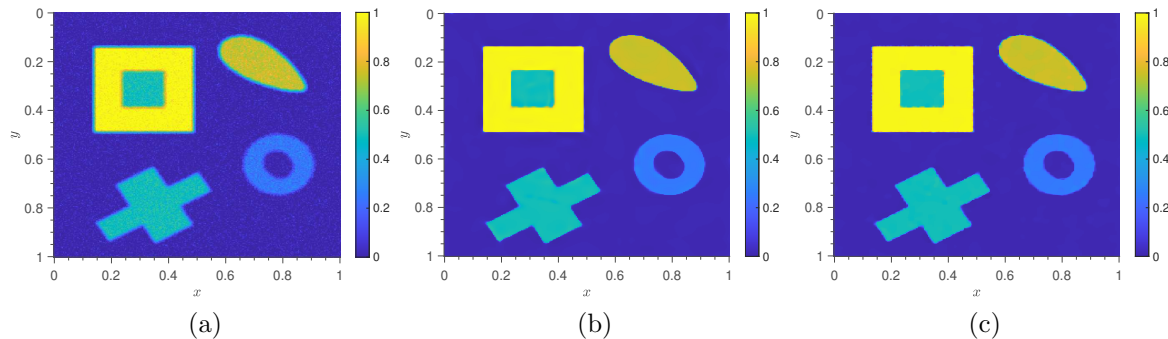


Figure 6: (a) Blurred and noisy image of four objects. (b) PaLEnTIR reconstruction and (c) TV reconstruction for the deconvolution problem.

Table 1: Performance Metrics of the Deconvolution Experiment

Method	Unknowns	PSNR	SNR	SSIM	MSE
PaLEnTIR	1125	32.7	24.4	53.4e-02	53.6e-05
TV	65536	31.2	22.9	52.6e-02	75.8e-05

4.2. X-ray Computed Tomography

X-ray computed tomography (CT) is typically well-approximated as a linear problem and is one of the most common and well-known methods for medical imaging applications. The forward model again takes the form of a matrix vector product, i.e., $\mathcal{M}(\mathbf{f}(\mathbf{p})) = \mathbf{R}\mathbf{f}(\mathbf{p})$ where \mathbf{R} denotes a (discrete) Radon transform, and the vector $\mathcal{M}(\mathbf{f}(\mathbf{p}))$ denotes the vectorized form of the sinogram data. In this paper, we explore the performance of PaLEnTIR on both two and three dimensional CT problems, focusing specifically on limited-angle and/or sparse view reconstructions.

For the first 2D CT experiment, we use an open-access data set of tomographic X-ray data of a carved cheese [43]. We note that, no approximation regarding the noise-level for this data set is given in [43]. The reference image, generated by the given high-resolution filtered back-projection (FBP) reconstruction, is the 2000×2000 pixels image shown in Figure 7a. In subsection 3.2, we considered the sparse view problem with 15 projections spanning the full 360 degree circle. Now, we consider a limited angle, limited view problem with 15 projections spanning the range $1^\circ - 90^\circ$. For this and the next CT experiments, there is a scaling and location difference between the provided high resolution filtered back-projection (FBP) and the CT data (which can be recognized from the recoveries); hence, we only provide a visual comparison of the TV and PaLEnTIR results for both 2D CT experiments. The 512×512 pixels PaLEnTIR and TV reconstructions of the carved cheese are shown in Figures 7b and 7c. The limited angle, limited view nature of the data exacerbates the difficulty of the reconstruction. For the TV recovery, we see X-Ray artifacts, resulting in blurred boundaries of the cheese and carved letters. Unintended artifacts in the background are also evident. The

PaLEnTIR recovery of the 262144 pixels image of the carved cheese is produced using a grid of only 8×8 basis functions. Consequently, the number of unknowns is almost 92% smaller than the number of unknowns required to solve for in a pixel-based method. The efficacy of the PaLEnTIR reconstruction is heavily influenced by the limitations of the available data, evident in imprecise boundaries at the top-left and bottom-right regions, similar to the errors in the TV recovery in these areas. However, in the remaining parts, PaLEnTIR demonstrates superior clarity and sharpness in both outer boundaries and intricate details around and within carved letters compared with the TV recovery.

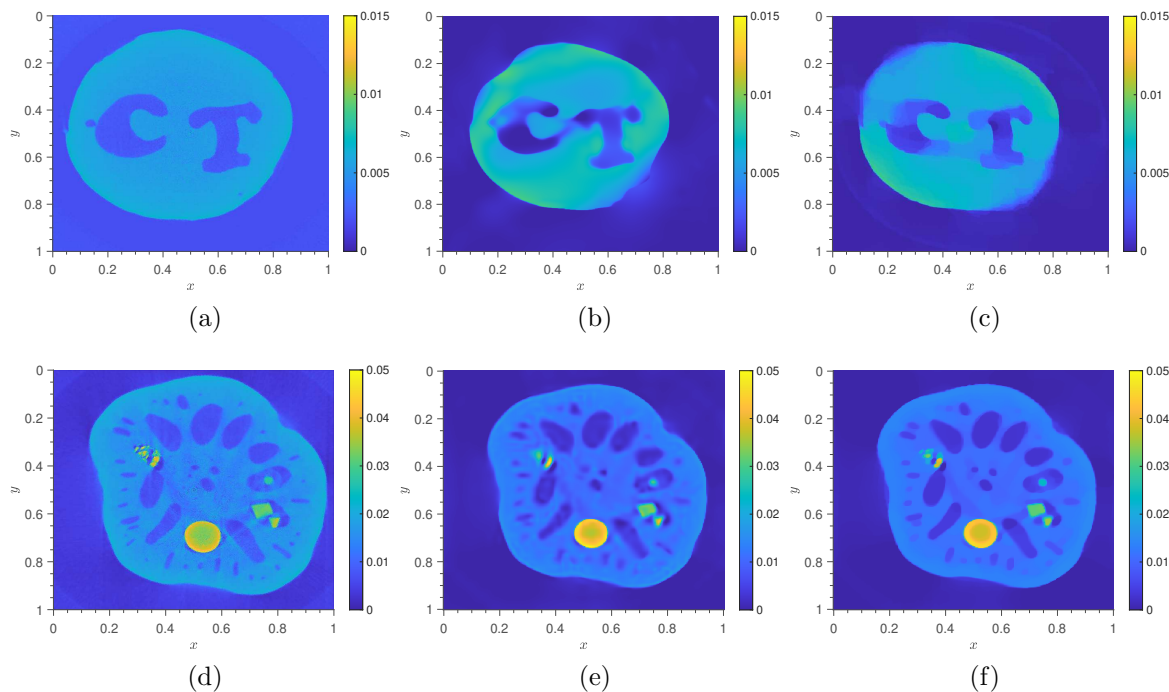


Figure 7: 2D Tomographic X-ray experiments: (a) Reference image of the carved cheese produced through high-resolution FBP reconstruction, computed from the full angle 360-projection sinogram. (b) PaLEnTIR limited angle and limited view reconstruction and (c) TV limited angle and limited view reconstruction of the carved cheese. (d) Reference image of the lotus root filled with attenuating objects, produced through high-resolution FBP reconstruction computed from the 360-projection sinogram. (e) Limited view PaLEnTIR reconstruction and (f) limited view TV reconstruction of the lotus root and the attenuating objects.

For the second 2D experiment, we use an open-access data set of tomographic X-ray data of a lotus root filled with attenuating objects [48]. Again, an approximate noise-level is not given in [48]. The lotus root, akin in texture to a potato, features an array of holes of varying sizes; as it is primarily composed of starch, its structural characteristics make it an ideal candidate for stuffing with diverse objects. The holes contain the following four objects, each in a distinct hole within the lotus root: a pencil, a piece of chalk, three rectangular ceramic pieces, and several match-heads.

Consequently, the lotus root, when filled with these objects, offers a diverse array of structures characterized by differing shapes, sizes, contrasts, and, notably, attenuations. This renders it a compelling subject for typical sparse-data CT applications [48]. The 1500×1500 pixels reference image, shown in Figure 7d, is generated from the high-resolution FBP reconstruction computed from the 360-projection sinogram provided in the dataset [48]. We consider a sparse view problem with 120 projections over the full range of angles. Figures 7e and 7f show the 256×256 pixels PaLEnTIR and TV reconstructions. The TV method requires a considerably larger number of unknowns, specifically 65536, for the reconstruction of a 256×256 image than our PaLEnTIR approach, which utilizes a set of 25×25 ABFs, amounting to only 3125 parameters. Remarkably, both methods demonstrate a good recovery of fine image details. Considering the recovery of the lotus root itself, the TV method yields a smoother reconstruction compared with the PaLEnTIR recovery. Both reconstructions exhibit a smooth background, free from X-ray artifacts and effectively represent all four objects placed within the lotus root’s hollows, even the smaller ones. Finally, it is worth highlighting that PaLEnTIR achieves the recovery of a fairly complex, multi-contrast, image from real X-ray data using a single level-set function; a feature that distinguishes it from existing level-set methods. Yet, as a PaLS method, PaLEnTIR captures an enormous amount of detail that is even hard to recognize in the reference image.

We now consider a 3D limited view parallel beam tomography experiment. We used TVReg [46] to construct the experimental setup. The true 3D image is of size $27 \times 27 \times 27$, shown in Figure 8a. The input data is formed from 31 projections, each having a plane center located on the surface of the $1/8$ of a Lebedev sphere [49]. Figure 8b illustrates the spatial distribution of projection plane centers for our 3D limited-angle view CT experiment. The objects of interest are represented in green, while the blue rings indicate the homogeneously spaced samples obtained from a Lebedev sphere centered at the origin. Notably, 31 of these blue rings are highlighted in red, indicating the selected projection plane centers for the experiment. These centers have been positioned to all reside within the same $1/8$ of the sphere, making the CT sparse and limited angle view.

The input data is corrupted with 1% additive Gaussian white noise. In this experiment, PaLEnTIR is constructed using 343 basis functions centered on a $7 \times 7 \times 7$ grid resulting in 3087 unknowns. We conduct a performance comparison between PaLEnTIR and L2-Total Variation (TV) regularization. The reconstructions by PaLEnTIR and TV are presented in Figures 8c and 8d, respectively, and the corresponding performance metrics are provided in Table 2. In the context of a limited-angle view 3D CT problem, both the PaLEnTIR and the TV method exhibit remarkable performance. Both methods produce high values for PSNR, SNR, and small values for MSE, with the TV method performing marginally better. The results for these metrics, all of which serve as critical metrics for assessing image quality and fidelity, emphasize the capacity for both methods to effectively reduce absolute error. Both methods attain the highest possible SSIM scores, a fact corroborated by the significant resemblance

between the reconstructed images in Figures 8c and 8d to the reference image shown in Figure 8a. PaLEnTIR maintains its advantage by recovering a 19683 pixel 3D image using only 3087 parameters, without the need of explicit regularization.

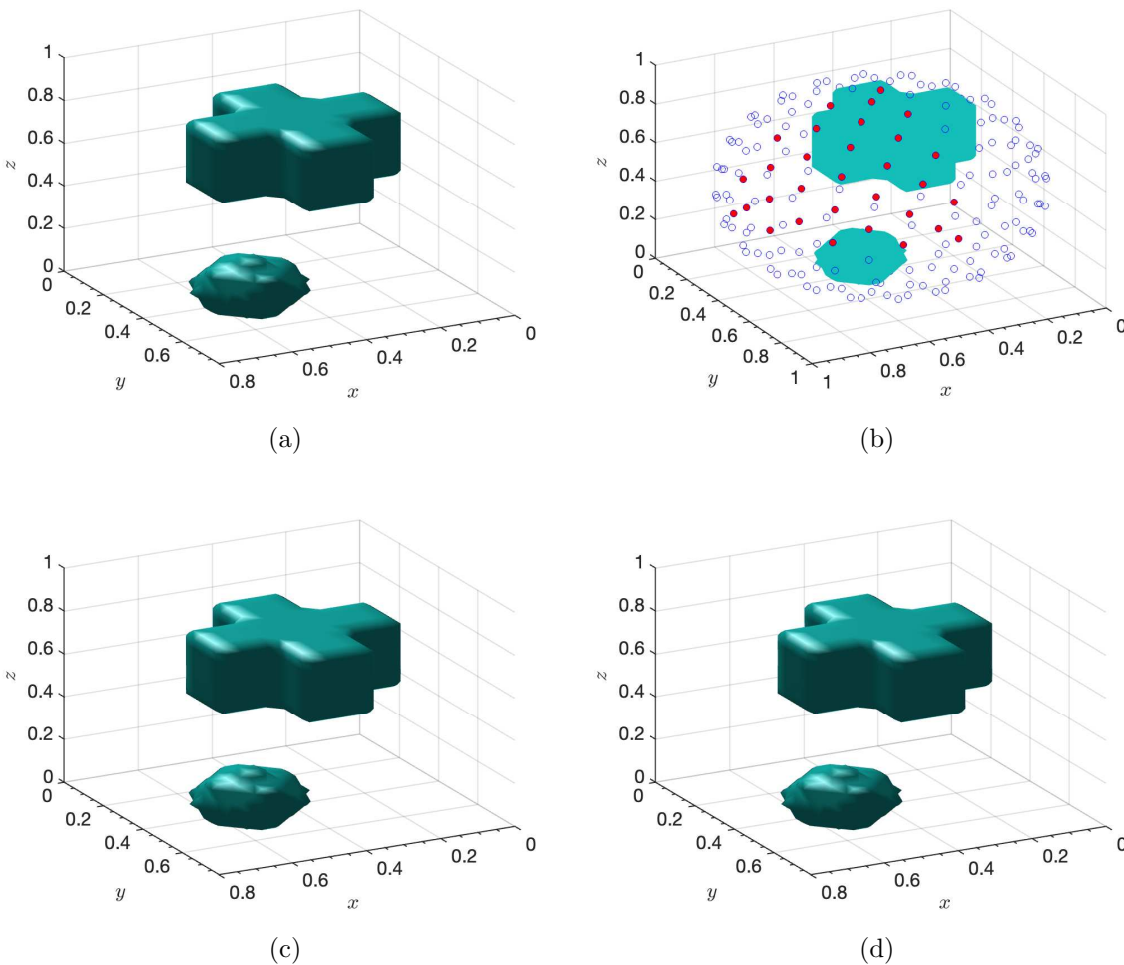


Figure 8: Results of 3D limited view parallel beam tomography experiment. (a) Original image of the 3D objects. (b) The distribution of projection plane centers. The 3D objects are represented in green, the blue points correspond to samples from a Lebedev sphere centered at the origin. The red points represent the selected samples from the sphere, chosen as the projection plane centers. (c) PaLEnTIR and (d) TV reconstructions.

Table 2: Performance Metrics of the 3D CT Experiment

Method	Unknowns	PSNR	SNR	SSIM	MSE
TV	19683	61.0	48.0	1.0	80.3e-08
PaLEnTIR	3087	60.1	47.2	1.0	96.9e-08

4.3. Diffuse Optical Tomography

Diffuse optical tomography (DOT) is a non-invasive, low-cost alternative for breast and brain imaging compared with X-ray and MRI [50]. In DOT, the tissue is illuminated with near-infrared light and the data, comprised of point measurements of diffused and partially absorbed photon fields, is collected external to the body. These measurements are used along with a mathematical model, typically a diffusion-absorption equation (posed in the frequency domain), to recover the optical absorption and (sometimes) scattering properties of the medium. Here we use such a model of the form

$$-\nabla \cdot (D(\mathbf{r})\nabla\eta(\mathbf{r})) + \mu(\mathbf{r}; \mathbf{p})\eta(\mathbf{r}) + \frac{i\omega}{\nu}\eta(\mathbf{r}) = g(\mathbf{r}), \quad (19)$$

where $D(\mathbf{r})$ represents the (here) known scalar diffusion at a point \mathbf{r} , $\mu(\mathbf{r}; \mathbf{p})$, the quantity for which we invert, represents the absorption as a function of space and the parameter vector \mathbf{p} , ω represents the modulation frequency of the light source, and ν represents the speed of light in the tissue. The sources are placed one grid point inside the medium [1], and the detectors are placed on the opposite boundary. On the boundaries where the sources and detectors are located, we have Robin boundary conditions; on the other boundaries, we use homogeneous Dirichlet boundary conditions, $\eta(\mathbf{r}) = 0$. For details, see [51, 52, 53]. The recovered absorption coefficient (and sometimes also the diffusion/scattering) can be used to characterize the state of the tissue [50, 54].

Following, e.g., [55], we assume that the absorption coefficient can be modeled via (8). As shown in Figure 9a, we take the region to be imaged as a rectangle of size 4cm by 4cm, with $m_s = 32$ sources arrayed on the right side and $m_d = 32$ detectors on the left. As before, we let $\mathbf{f}(\mathbf{p})$ denote the discrete absorption image for a given parameter vector, that is, $[\mathbf{f}(\mathbf{p})]_i = f(\mathbf{r}_i, \mathbf{p})$ for any grid point \mathbf{r}_i . Assuming we collect data for all detectors when each source is active, we obtain a data vector \mathbf{d} with $m = m_s \times m_d$ values for each modulation frequency ω .

The input-output map from sources to detectors [56] (also called the *transfer function*) as a function of \mathbf{p} and ω , is given by

$$\Psi(\mathbf{f}(\mathbf{p}); \omega) = \mathbf{C}^T \mathbf{A}(\mathbf{f}(\mathbf{p}); \omega)^{-1} \mathbf{B} \in \mathbb{R}^{m_d \times m_s}, \quad (20)$$

where $\mathbf{B} \in \mathbb{R}^{n \times m_s}$ represents m_s sources, n is the total number of voxels or grid points, $\mathbf{A}(\mathbf{f}(\mathbf{p}); \omega) \in \mathbb{R}^{n \times n}$ represents the discretization of the diffusion-absorption equation, and $\mathbf{C}^T \in \mathbb{R}^{m_d \times n}$ simulates the measurement of outputs at m_d detectors. So, $\mathbf{A}(\mathbf{f}(\mathbf{p}); \omega)\mathbf{X} = \mathbf{B}$ represents the discretized PDE that relates photon fluence/flux at grid points to the sources [1]. The DOT inverse problem is then specified by the forward mapping $\mathcal{M}(\mathbf{f}(\mathbf{p}); \omega) = \text{vec}(\Psi(\mathbf{f}(\mathbf{p}); \omega))$, the vectorization of the transfer function outputs for a vector of frequencies $\boldsymbol{\omega} = [\omega_1, \dots, \omega_{m_f}]$. Given a vector of measured data (with additive noise) \mathbf{d} , we solve for \mathbf{p} by minimizing $\frac{1}{2}\|\text{vec}(\Psi(\mathbf{f}(\mathbf{p}); \omega)) - \mathbf{d}\|_2^2$. Note that regularization is provided implicitly by the parameterization.

We present results in Figure 9, with the true anomaly shown in Figure 9a, and we focus on the quality of the shape reconstruction using the new PaLEnTIR

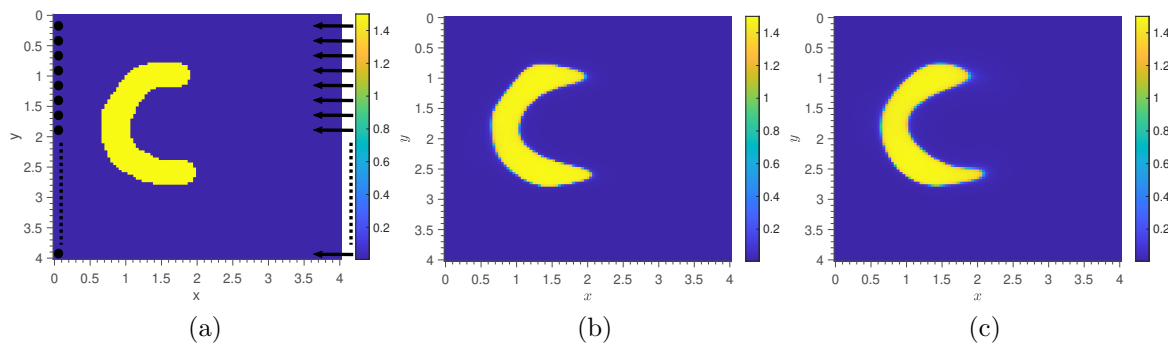


Figure 9: The results of Diffuse Optical Tomography experiment are shown. (a) True anomaly with sources (right) and Detectors (left), (b) reconstruction of the absorption image without additive white noise (SSIM:0.92, MSE:1.46e-2, PSNR:21.87dB, SNR:10.75dB), (c) reconstruction of the absorption image with 1% additive white noise (SSIM:0.89, MSE:1.92e-2, PSNR:20.69dB, SNR:9.57dB).

parameterization. The DOT problem is severely ill-posed, due to both the limited numbers of sources and detectors and the highly diffuse nature of the problem, so accurate reconstructions are not possible. Indeed, this is why the shape-based parameterized reconstruction for problems with well-defined boundaries is important. To distinguish between reconstruction error due to noise as well as ill-posedness and reconstruction error due to the nature of the problem, we provide a reconstruction with 1% additive Gaussian white noise (realistic) as well as one without noise. The latter serves to demonstrate the difficulty of the data limited problem which should be distinguished from the approximation quality of PaLEnTIR. For both PaLEnTIR recoveries, $11^2 = 121$ ABFs are used and contrast coefficients are chosen as minimum and maximum values of the ground-truth image. The performance metrics are given in the figure description for both recoveries. The reconstruction for the data without noise is shown in Figure 9b. The model captures the structure quite well with SSIM score of 0.92, with slight imperfections due to the data limited nature of the problem rather than the PaLEnTIR model. When additive noise is added and we run the algorithm we observe the image in Figure 9c. While the edges are slightly less clear in the noisy case, the reconstruction is remarkably good with SSIM score of 0.89, given the limitations of the data and the diffusive nature of the forward problem. It is important to note that there was no parameter to tune in generating this reconstruction.

5. Conclusion and Future Work

In this paper, we redefine the parametric level-set method to enhance the quality and functionality of the PaLS approach in the context of solving inverse imaging problems for images with (possibly multiple) piecewise constant contrasts. As the most significant contribution of our work, the PaLEnTIR parameterization stands out as the only level-

set approach, as far as we know, that employs only a single level-set function, irrespective of the number of contrasts or their values. Thus PaLEnTIR can represent multi-contrast scenes with very few parameters compared with traditional level-set based and pixel-based methods, and without any need to tune a regularization parameter. We investigate the qualitative performance of our new model and demonstrate that replacing RBFs in PaLS with ABFs expands the family of shapes that can be represented by a single basis function from circles to rotated ellipses. Relative to RBF PaLS, PaLEnTIR demonstrates a better reconstruction capability by capturing significantly more details, by converging much faster, and by achieving significantly lower objective function values. We empirically demonstrate how PaLEnTIR outperforms the RBF PaLS in terms of the condition number in both single and multiple basis functions cases.

We demonstrate the utility of PaLEnTIR on numerical experiments over a range of inverse problems, including 2D and 3D experiments, real data, and both non-linear and linear inverse problems. In the examples where comparisons are made, PaLEnTIR reconstructions are about as good or somewhat better than those computed with competing reconstruction methods, whose parameters have been manually tuned to minimize the MSE, which is not possible in practice. The built-in regularization through the parameterization allows, even in the non-linear, severely data-limited DOT problem, for high-quality reconstructions. Multiple contrasts in varying shapes and configurations are readily picked up by our new approach without any hand-tuning or regularization parameter selection. In summary, we have demonstrated the power of PaLEnTIR for reconstruction, denoising, and restoration for the class of piecewise constant images.

The performance exhibited by PaLEnTIR opens up prospects for future research in several key areas. Our forthcoming work will comprehensively explore the application of PaLEnTIR to three-dimensional domains, subjecting the model to diverse nonlinear and ill-posed problems. While the current use of homogeneously distributed basis functions has proven effective, we envision further enhancements by incorporating an adaptive refinement strategy, akin to strategies proposed in [57, 58], which place additional basis functions in regions of higher geometric complexity. Additionally, our research agenda includes a focused investigation into the application of PaLEnTIR for uncertainty quantification. This entails the development of prior models for PaLEnTIR parameters based on object priors, with a specific emphasis on leveraging these priors to quantify accuracy in tasks such as object localization and characterization throughout the recovery process.

Appendix A. Derivatives of the 2D PaLEnTIR parameterization with respect to model parameters

The TREGS algorithm necessitates a function for computing the Jacobian matrix. In this section, we present the derivations essential for calculating the Jacobian of the PaLEnTIR model, denoted as $f(\mathbf{r}; \mathbf{p})$. Since \mathbf{p} encompasses both anisotropic basis function (ABF) parameters and contrast parameters, we represent these parameters

with two separate vectors: $\hat{\mathbf{p}}$ for the ABF parameters and \mathbf{p}_c for the contrast parameters. The PaLEnTIR model, now expressed as $f(\mathbf{r}; \hat{\mathbf{p}}, \mathbf{p}_c)$, is defined as:

$$f(\mathbf{r}; \hat{\mathbf{p}}; \mathbf{p}_c) = C_\Delta(\mathbf{r}; \mathbf{p}_c)T(\phi(\mathbf{r}; \hat{\mathbf{p}})) + C_L(\mathbf{r}; \mathbf{p}_c). \quad (\text{A.1})$$

Here $C_\Delta(\mathbf{r}; \mathbf{p}_c) = C_H(\mathbf{r}; \mathbf{p}_c) - C_L(\mathbf{r}; \mathbf{p}_c)$. We begin by examining the derivatives with respect to $\hat{\mathbf{p}}$. The derivative of $f(\mathbf{r}; \hat{\mathbf{p}}; \mathbf{p}_c)$ with respect to a parameter \hat{p}_i , that is the i^{th} parameter in $3N$ -vector $\hat{\mathbf{p}}$, is expressed using the chain rule as:

$$\frac{\partial f(\mathbf{r}; \hat{\mathbf{p}}; \mathbf{p}_c)}{\partial \hat{p}_i} = C_\Delta(\mathbf{r}; \mathbf{p}_c)T'(\phi(\mathbf{r}; \hat{\mathbf{p}}))\frac{\partial \phi(\mathbf{r}; \hat{\mathbf{p}})}{\partial p_i}. \quad (\text{A.2})$$

The first factor on the right side in (A.2) is the difference between the contrast coefficients. The second term is the derivative of the transition function. The transition function for a c -level-set, $T(x)$, is defined as:

$$T(x) = \frac{1}{2} \left[1 + \frac{2}{\pi} \tan^{-1} \left(\frac{\pi(x-c)}{w} \right) \right], \quad (\text{A.3})$$

and the derivative of (A.3) is given by:

$$T'(\phi(\mathbf{r}; \hat{\mathbf{p}})) = \frac{1}{w} \left[\frac{1}{1 + \left(\frac{\pi x}{w} \right)^2} \right]. \quad (\text{A.4})$$

The third factor in (A.2) is the derivative of the parametric level-set function, ϕ , with respect to model parameters. ϕ is defined in (9). The expressions for the derivatives of (9) with respect to each parameter are provided below, where elements $[\alpha_j; \beta_j; \gamma_j]$ correspond to the parameters of the j^{th} ABF for $j = 1, 2 \dots N$:

$$\frac{\partial \phi(\mathbf{r}; \hat{\mathbf{p}})}{\partial \alpha_j} = \frac{\partial \sigma_h(\alpha_j)}{\partial \alpha_j} \psi(\mathbf{R}_j(\mathbf{r} - \boldsymbol{\chi}_j)), \quad (\text{A.5})$$

$$\frac{\partial \phi(\mathbf{r}; \hat{\mathbf{p}})}{\partial \beta_j} = \sigma_h(\alpha_j) \frac{\partial \psi(\mathbf{R}_j(\mathbf{r} - \boldsymbol{\chi}_j))}{\partial \beta_j}, \quad (\text{A.6})$$

$$\frac{\partial \phi(\mathbf{r}; \hat{\mathbf{p}})}{\partial \gamma_j} = \sigma_h(\alpha_j) \frac{\partial \psi(\mathbf{R}_j(\mathbf{r} - \boldsymbol{\chi}_j))}{\partial \gamma_j}. \quad (\text{A.7})$$

The derivatives with respect to parameters in the equations above are defined as:

$$\frac{\partial \sigma_h(\alpha_j)}{\partial \alpha_j} = \frac{1}{2} \text{sech}^2\left(\frac{\alpha_j}{2}\right), \quad (\text{A.8})$$

$$\frac{\partial \psi(\mathbf{R}_j \mathbf{r}_\Delta)}{\partial \beta_j} = (-2\mu^2) \psi(\mathbf{R}_j \mathbf{r}_\Delta) \mathbf{r}_\Delta^T \begin{bmatrix} e^{2\beta} & 0 \\ \gamma e^\beta & -e^{-\beta} \end{bmatrix} \mathbf{r}_\Delta, \quad (\text{A.9})$$

$$\frac{\partial \psi(\mathbf{R}_j \mathbf{r}_\Delta)}{\partial \gamma_j} = (-\mu^2) \psi(\mathbf{R}_j \mathbf{r}_\Delta) \mathbf{r}_\Delta^T \begin{bmatrix} 0 & e^\beta \\ e^\beta & 2\gamma \end{bmatrix} \mathbf{r}_\Delta. \quad (\text{A.10})$$

where $\mathbf{r}_\Delta = (\mathbf{r} - \boldsymbol{\chi}_j)$. Next, the derivative of $f(\mathbf{r}; \hat{\mathbf{p}}; \mathbf{p}_c)$ with respect to \mathbf{p}_c is defined as

$$\frac{\partial f(\mathbf{r}; \hat{\mathbf{p}}; \mathbf{p}_c)}{\partial p_{c_k}} = C_\Delta(\mathbf{r}; \mathbf{e}_k)T(\phi(\mathbf{r}; \hat{\mathbf{p}})) + C_L(\mathbf{r}; \mathbf{e}_k), \quad (\text{A.11})$$

where $\mathbf{e}_k \in \mathbb{R}^{2N}$ is a $2N$ -vector with its k^{th} element equal to 1 and all other elements equal to 0, for $k = 1, 2 \dots 2N$.

References

- [1] S. .R. Arridge. Optical tomography in medical imaging. *Inverse Problems*, Vol. 16:R41–R93, 1999.
- [2] Sarah Fakhreddine, Jonghyun Lee, Peter Kitanidis, Scott Fendorf, and Massimo Rolle. Imaging geochemical heterogeneities using inverse reactive transport modeling: An example relevant for characterizing arsenic mobilization and distribution. *Advances in Water Resources*, 88, 12 2015.
- [3] Gad El-Qady, Mahfooz Hafez, M.A. Abdalla, and K. Ushijima. Imaging subsurface cavities using geoelectric tomography and ground-penetrating radar. *Journal of Cave and Karst Studies*, 67:174–181, 12 2005.
- [4] I.T. Rekanos, T.V. Yioultis, and T.D. Tsiboukis. Inverse scattering using the finite-element method and a nonlinear optimization technique. *IEEE Transactions on Microwave Theory and Techniques*, 47(3):336–344, 1999.
- [5] Andreas Kirsch. Characterization of the shape of a scattering obstacle using the spectral data of the far field operator. *Inverse Problems*, 14(6):1489, dec 1998.
- [6] Fadil Santosa. A level-set approach for inverse problems involving obstacles . *ESAIM: Control, Optimisation and Calculus of Variations*, 1:17–33, 1996.
- [7] Alireza Aghasi, Misha Kilmer, and Eric L. Miller. Parametric Level Set Methods for Inverse Problems. *SIAM Journal on Imaging Sciences*, 4(2):618–650, 2011.
- [8] Stanley Osher and James A Sethian. Fronts propagating with curvature-dependent speed: Algorithms based on Hamilton-Jacobi formulations. *Journal of Computational Physics*, 79(1):12–49, 1988.
- [9] Oliver Dorn and Dominique Lesselier. Level set methods for inverse scattering. *Inverse Problems*, 22:R67, 06 2006.
- [10] Haihua Feng, William Karl, and David Castanon. A curve evolution approach to object-based tomographic reconstruction. *IEEE transactions on image processing : a publication of the IEEE Signal Processing Society*, 12:44–57, 02 2003.
- [11] T.F. Chan and L.A. Vese. Active contours without edges. *IEEE Transactions on Image Processing*, 10(2):266–277, 2001.
- [12] Kees van den Doel and U. Ascher. On level set regularization for highly ill-posed distributed parameter estimation problems. *Journal of Computational Physics*, 216:707–723, 08 2006.
- [13] Stanley J. Osher and Fadil Santosa. Level Set Methods for Optimization Problems Involving Geometry and Constraints: I. Frequencies of a Two-Density Inhomogeneous Drum. *Journal of Computational Physics*, 171(1):272–288, 2001.
- [14] Michael McMillan, Christoph Schwarzbach, Eldad Haber, and Douglas Oldenburg. Multiple body parametric inversion of frequency-and time-domain airborne electromagnetics. In *SEG Technical Program Expanded Abstracts 2016*, pages 846–851. Society of Exploration Geophysicists, 2016.
- [15] Ajinkya Kadu, Tristan van Leeuwen, and Wim A. Mulder. Salt Reconstruction in Full-Waveform Inversion With a Parametric Level-Set Method. *IEEE Transactions on Computational Imaging*, 3(2):305–315, 2017.
- [16] GM Hoversten, C Schwarzbach, P Belliveau, Eldad Haber, and R Shekhtman. Borehole to surface electromagnetic monitoring of hydraulic fractures. In *79th EAGE Conference and Exhibition 2017*, volume 2017, pages 1–5. European Association of Geoscientists & Engineers, 2017.
- [17] Fitsum Mesadi, Mujdat Cetin, and Tolga Tasdizen. Disjunctive normal level set: An efficient parametric implicit method. In *2016 IEEE International Conference on Image Processing (ICIP)*, pages 4299–4303. IEEE, 2016.
- [18] Naren Naik, Rick Beatson, and Jerry Eriksson. Radial-basis-function level-set-based regularized Gauss–Newton-filter reconstruction scheme for dynamic shape tomography. *Applied Optics*, 53, 10 2014.
- [19] Zhi-Tian Niu, Hong Qi, Ze-Yu Zhu, Ke-Fu Li, Ya-Tao Ren, and Ming-Jian He. A novel parametric level set method coupled with tikhonov regularization for tomographic laser absorption

- reconstruction. *Applied Thermal Engineering*, 201:117819, 2022.
- [20] Haytham A. Ali and Hiroyuki Kudo. Level-Set Method for Limited-Data Reconstruction in CT using Dictionary-Based Compressed Sensing. In *2023 15th International Conference on Computer and Automation Engineering (ICCAE)*, pages 264–268, 2023.
- [21] Gabriele Incorvaia and Oliver Dorn. Stochastic Optimization Methods for Parametric Level Set Reconstructions in 2D through-the-Wall Radar Imaging. *Electronics*, 9(12), 2020.
- [22] Moshe Eliasof, Andrei Sharf, and Eran Treister. Multimodal 3D Shape Reconstruction under Calibration Uncertainty Using Parametric Level Set Methods. *SIAM Journal on Imaging Sciences*, 13(1):265–290, 2020.
- [23] Alex Hiles and Oliver Dorn. Colour level set regularization for the electromagnetic imaging of highly discontinuous parameters in 3D*. *Inverse Problems in Science and Engineering*, 29:1–36, 07 2020.
- [24] Hong-Kai Zhao, T. Chan, B. Merriman, and S. Osher. A Variational Level Set Approach to Multiphase Motion. *Journal of Computational Physics*, 127(1):179–195, 1996.
- [25] J. Lie, M. Lysaker, and Xue-Cheng Tai. A binary level set model and some applications to Mumford-Shah image segmentation. *IEEE Transactions on Image Processing*, 15(5):1171–1181, 2006.
- [26] Dong Liu, Danny Smyl, and Jiangfeng Du. Nonstationary Shape Estimation in Electrical Impedance Tomography Using a Parametric Level Set-Based Extended Kalman Filter Approach. *IEEE Transactions on Instrumentation and Measurement*, 69(5):1894–1907, 2020.
- [27] Oguz Semerci and Eric Miller. A Parametric Level Set Approach to Simultaneous Object Identification and Background Reconstruction for Dual Energy Computed Tomography. *IEEE transactions on image processing : a publication of the IEEE Signal Processing Society*, 21:2719–34, 05 2012.
- [28] Maokun Li, Aria Abubakar, and Tarek M. Habashy. A three-dimensional model-based inversion algorithm using radial basis functions for microwave data. *IEEE Transactions on Antennas and Propagation*, 60(7):3361–3372, 2012.
- [29] Ralph A. Willoughby. Solutions of Ill-Posed Problems (A. N. Tikhonov and V. Y. Arsenin). *SIAM Review*, 21(2):266–267, 1979.
- [30] M Ben, Mohamed Khames Ben Hadj Miled, and Eric Miller. A projection-based level-set approach to enhance conductivity anomaly reconstruction in electrical resistance tomography. *Inverse Problems*, 23:2375–2400, 12 2007.
- [31] Rui Guo, Zekui Jia, Xiaoqian Song, Maokun Li, Fan Yang, Shenheng Xu, and Aria Abubakar. Pixel- and model-based microwave inversion with supervised descent method for dielectric targets. *IEEE Transactions on Antennas and Propagation*, 68(12):8114–8126, 2020.
- [32] Rui Li, Yongfu Zhang, Lihui Peng, and Xinghe Liao. An Image Reconstruction For Electrical Capacitance Tomography Using Parametric Level Set. In *2020 5th International Conference on Computer and Communication Systems (ICCCS)*, pages 384–390, 2020.
- [33] Dong Liu, Anil Kumar Khambampati, and Jiangfeng Du. A parametric level set method for electrical impedance tomography. *IEEE Transactions on Medical Imaging*, 37(2):451–460, 2018.
- [34] Oliver Dorn and Dominique Lesselier. *Level Set Techniques For Structural Inversion In Medical Imaging*, pages 61–90. Springer New York, New York, NY, 2007.
- [35] Eric de Sturler and Misha Kilmer. A Regularized Gauss–Newton Trust Region Approach to Imaging in Diffuse Optical Tomography. *SIAM J. Scientific Computing*, 33:3057–3086, 01 2011.
- [36] Andrew R. Conn, Nicholas I. M. Gould, and Philippe L. Toint. *Trust Region Methods*. Society for Industrial and Applied Mathematics, 2000.
- [37] Per Christian Hansen. *Rank-Deficient and Discrete Ill-Posed Problems*. Society for Industrial and Applied Mathematics, 1998.
- [38] Yanyan Shi, Xiaolong Kong, Meng Wang, Yuehui Wu, and Lan Yang. A Non-Convex L1-Norm Penalty-Based Total Generalized Variation Model for Reconstruction of Conductivity Distribution. *IEEE Sensors Journal*, 20(14):8137–8146, 2020.

- [39] Michael Yu Wang and Xiaoming Wang. “Color” level sets: a multi-phase method for structural topology optimization with multiple materials. *Computer Methods in Applied Mechanics and Engineering*, 193(6):469–496, 2004.
- [40] G. Allaire, C. Dapogny, G. Delgado, and G. Michailidis. Multi-phase structural optimization via a level set method. *ESAIM: Control, Optimisation and Calculus of Variations*, 20(2):576–611, 2014.
- [41] R. Keys. Cubic convolution interpolation for digital image processing. *IEEE Transactions on Acoustics, Speech, and Signal Processing*, 29(6):1153–1160, 1981.
- [42] Francois Lekien and J Marsden. Tricubic interpolation in three dimensions. *International Journal for Numerical Methods in Engineering*, 63(3):455–471, 2005.
- [43] Tatiana A. Bubba, Markus Juvonen, Jonatan Lehtonen, Maximilian März, Alexander Meaney, Zenith Purisha, and Samuli Siltanen. Tomographic X-ray data of carved cheese. *arXiv*, abs/1705.05732, 2017.
- [44] Stephen J. Wright Jorge Nocedal. *Numerical Optimization*. Springer New York, NY, second edition, 2006.
- [45] Nicholas J. Higham. *Accuracy and Stability of Numerical Algorithms*. Society for Industrial and Applied Mathematics, second edition, 2002.
- [46] Tobias Lindstrøm Jensen, Jakob Heide Jørgensen, Per Christian Hansen, and Søren Holdt Jensen. *Tvreg*, 2010.
- [47] Zhou Wang, A.C. Bovik, H.R. Sheikh, and E.P. Simoncelli. Image quality assessment: from error visibility to structural similarity. *IEEE Transactions on Image Processing*, 13(4):600–612, 2004.
- [48] Tatiana A. Bubba, Andreas Hauptmann, Simo Huotari, Juho Rimpeläinen, and Samuli Siltanen. Tomographic X-ray data of a lotus root filled with attenuating objects. *ArXiv*, abs/1609.07299, 2016.
- [49] Vyacheslav Ivanovich Lebedev. Quadratures on a sphere. *USSR Computational Mathematics and Mathematical Physics*, 16(2):10–24, 1976.
- [50] DA Boas, DH Brooks, EL Miller, CA DiMarzio, M. Kilmer, RJ Gaudette, and Q. Zhang. Imaging the body with diffuse optical tomography. *IEEE Signal Processing Magazine*, 18(6):57–75, 2001.
- [51] Eric de Sturler, Serkan Gugercin, Misha E. Kilmer, Saifon Chaturantabut, Christopher Beattie, and Meghan O’Connell. Nonlinear Parametric Inversion Using Interpolatory Model Reduction. *SIAM J. Sci. Comput*, 37(3):B495–B517, 2015.
- [52] Selin S. Aslan, Eric de Sturler, and Misha E. Kilmer. Randomized approach to nonlinear inversion combining random and optimized simultaneous sources and detectors. *SIAM J. Sci. Comput*, 41:B229–B249, 2019.
- [53] Athanasios Constantinos Antoulas, Christopher Andrew Beattie, and Serkan Güğercin. *Interpolatory methods for model reduction*. SIAM, 2020.
- [54] Qianqian Fang, Stefan A Carp, Juliette Selb, Greg Boverman, Quan Zhang, Daniel B Kopans, Richard H Moore, Eric L Miller, Dana H Brooks, David Boas, et al. Combined optical imaging and mammography of the healthy breast: optical contrast derived from breast structure and compression. *Medical Imaging, IEEE Transactions on*, 28(1):30–42, 2009.
- [55] Fridrik Larusson, Sergio Fantini, and Eric L Miller. Parametric level set reconstruction methods for hyperspectral diffuse optical tomography. *Biomedical optics express*, 3(5):1006–1024, 2012.
- [56] Arvind K. Saibaba, Pranjali Prasad, Eric de Sturler, Eric Miller, and Misha E. Kilmer. Randomized approaches to accelerate MCMC algorithms for Bayesian inverse problems. *Journal of Computational Physics*, 440:110391, 2021.
- [57] Alexandre Baussard, Eric L Miller, and Denis Prémel. Adaptive B-spline scheme for solving an inverse scattering problem. *Inverse Problems*, 20(2):347, jan 2004.
- [58] Alexandre Baussard, Eric L Miller, and Dominique Lesselier. Adaptive multiscale reconstruction of buried objects. *Inverse Problems*, 20(6):S1, nov 2004.